



A new active contour model driven by pre-fitting bias field estimation and clustering technique for image segmentation

Guirong Weng*, Bin Dong

School of Mechanical and Electric Engineering, Soochow University, Suzhou 215021, China



ARTICLE INFO

Keywords:

Active contour model
Bias field
K-means++
Intensity inhomogeneity
Image segmentation

ABSTRACT

Due to uneven illumination or limitations of imaging devices, intensity inhomogeneities are more or less present in images obtained by different imaging modes. This ubiquitous intensity inhomogeneity makes image segmentation more difficult. This paper proposes a new bias field model (KPBFE) based on pre-fitting bias field estimation to deal with intensity inhomogeneity in the image segmentation. A new function for computing bias field b is proposed with K-means++ clustering algorithm. The computation method of clustering center points takes into account the average value of the grayscale within the contour of the bias field estimation and outside the contour. Meanwhile, we use a variational level set function with arctan function and a new adaptive function τ to limit the magnitude of the data driver term. Since the computation of bias field estimation is completed before the iteration and there is no convolution operation in the process, the computing speed of the proposed model is greatly increased. Experiments results show that our model can effectively segment the images with intensity inhomogeneity. Compared with some classical models, our method also has faster computation speed, higher segmentation accuracy and better initial robustness.

1. Introduction

Image segmentation is an important part in the field of image processing and computer vision. It is widely used in many fields, including industrial automation production, medical image analysis, intelligent monitoring and traffic management. In the past decades, various image segmentation methods were proposed (Wu and Kang, 2021; Mousavirad et al., 2020; Sarkar et al., 2016; Çataloluk and Çelebi, 2018; Li et al., 2006; Gamino-Sánchez et al., 2018; Demirhan and Güler, 2011; Jin and Weng, 2019; Cai et al., 2018; Chan et al., 2018; Banerjee and Maji, 2019). Active contour model (ACM) is one of the most representative image segmentation methods since Kass et al. (2011) proposed. Active contour model can obtain subpixel level accuracy of the target boundary and provide a smooth closed contour as the segmentation result (Miao et al., 2018). Therefore, it is suitable for scenes requiring high segmentation accuracy, such as detecting the shape and size of lesions, locating damaged areas of industrial machines, automatic segmentation and identification of vehicle license plates, etc (Pham et al., 2016; Comelli et al., 2019). In addition, the introduction of level set method (Li et al., 2010) promotes the development of active contour model. Nowadays it is also a research hotspot in image segmentation. Traditional active contour models can be classified as: edge-based models (Li et al., 2010, 2016; Liu et al.,

2017; Zhou et al., 2015) and region-based models (Wang et al., 2009; Zhang et al., 2010; Chan and Vese, 1997; Li et al., 2008).

The most widely used active contour model is region-based models. There are usually some interferences in image segmentation, such as uneven illumination, noise, shadow and intensity inhomogeneity. These disturbances bring great difficulties to image segmentation. Traditional region-based models are not ideal enough to guarantee segmentation accuracy and speed simultaneously for intensity inhomogeneity image. Another kind of region-based segmentation method is called bias field model. The bias correction (BC) model (Li et al., 2011) and the LSACM model (Zhang et al., 2016) are two classical bias field models. The BC model has strong robustness to the initial contour. Nevertheless, too much convolution computation in iteration results in slow segmentation speed. The LSACM model has a good segmentation effect for images with intensity inhomogeneity. However, it still fails to solve the problems of initial contour sensitivity and slow segmentation speed. The CLSM model proposed by Zhou et al. (Zhou et al., 2017) in 2017 allows flexible initializations and can segment images effectively with both noise and intensity inhomogeneity. Its defect is a kernel function leads to long segmentation time. Wang et al. proposed the EFI model (Wang et al., 2018) to deal with images with intensities inhomogeneous and estimate their bias fields with a high performance. However, the convolution computation in this model still increases the iteration time.

* Correspondence to: School of Mechanical and Electric Engineering, Soochow University, No. 178, Ganjiang Road, Suzhou City, Jiangsu Province, 215021, China.

E-mail addresses: wgr@suda.edu.cn (G. Weng), 20184229019@stu.suda.edu.cn (B. Dong).

Table 1 briefly summarizes the characteristics of the above four bias field models.

In this paper, we propose a new active contour model (KPBFE) to compute the estimation of bias field and overcome the shortcomings of the BC model and the LSACM model. Firstly, we use K-means++ clustering algorithm to cluster multivariable data and take the clustering center point as bias field b . The computation method of clustering center points takes the average value of the grayscale within and outside the contour into account. The function of clustering center can be regarded as a special case of the CV model. Then we minimize the energy function. We optimize a variational level set function with different data driven term. A new adaptive function τ is used to limit the magnitude of the data driver term. Finally, we compute gradient flow function and complete the computation. The computation of bias field value b is completed before the iteration. There is no convolution operation in the computing process, so the computation speed is greatly increased. Experiments results show that our model has faster segmentation speed and better robustness on the images with intensity inhomogeneity.

The rest of this paper is organized as follows. We introduce the research background in Section 2. The proposed model is shown in Section 3. Section 4 is experiments. Section 5 includes several discussions. The conclusion is in Section 6.

2. Background

Taking the intensity inhomogeneity in image segmentation into consideration, the real image can be built into a composite image model (Wells et al., 1995; Li et al., 2014), which is given as follows:

$$I(\mathbf{x}) = b(\mathbf{x})J(\mathbf{x}) + n(\mathbf{x}) \quad (1)$$

This model decomposes grayscale inhomogeneity into a component of the image. Where $b(\mathbf{x})$ is the component of intensity inhomogeneity, which is called the bias field, $J(\mathbf{x})$ is the real image, and $n(\mathbf{x})$ is the additional noise. Fig. 1 is a schematic diagram of this image model. The real image $J(\mathbf{x})$ reflects the intrinsic physical properties of the image. So it can be assumed to be an approximate fitting constant. The bias field $b(\mathbf{x})$ is assumed to be slowly varying and the additional noise $n(\mathbf{x})$ is assumed to be zero mean Gaussian noise.

The real image and bias field hypothesis are concretely described as follows:

Assumption (1). The bias field b changes slowly in the neighborhood of each point in the image domain. We can think of b as a constant.

Assumption (2). N different fitting constants c_1, \dots, c_N are taken by real image $J(\mathbf{x})$ in the disjoint regions $\{\Omega_i\}_{i=1}^N$. Where $\{\Omega_i\}_{i=1}^N$ can be divided into image domain partition $\Omega = \cup_{i=1}^N \Omega_i$ and $\Omega_i \cap \Omega_j = \emptyset, (i \neq j)$. This image model has been widely accepted in most bias field models. The proposed model also use this image model.

In 2011, Li et al. proposed the BC model and deduced the following energy function for the point (\mathbf{x}, \mathbf{y}) in the image domain by the local clustering criterion function:

$$\varepsilon \triangleq \int \left(\sum_{i=1}^N \int_{\Omega_i} K(\mathbf{y} - \mathbf{x}) |I(\mathbf{x}) - b(\mathbf{y})c_i|^2 d\mathbf{x} \right) d\mathbf{y} \quad (2)$$

where $b(\mathbf{y})$ is bias field estimation and c_i is constant. The truncated Gaussian function K is selected as the kernel function, which can be expressed as:

$$K(\mathbf{u}) = \begin{cases} \frac{1}{\alpha} e^{-|\mathbf{u}|^2/2\sigma^2}, & \text{for } |\mathbf{u}| \leq \rho \\ 0, & \text{otherwise} \end{cases} \quad (3)$$

where α is a normalized constant, σ is the standard deviation of the Gaussian function, ρ is the radius of the neighborhood O_y and $\int K(\mathbf{u})d\mathbf{u} = 1$.

For the region in Eq. (2), it is called two-phase energy function when $N = 2$. When $N > 2$ it is called the multiphase energy function.

In the case of two-phase, the image domain Ω can be split into two disjoint regions Ω_1 and Ω_2 . Then represent regions Ω_1 and Ω_2 with their membership functions $M_1(\phi) = H_\epsilon(\phi)$ and $M_2(\phi) = 1 - H_\epsilon(\phi)$, Where $H_\epsilon(\phi)$ is Heaviside function. Then Eq. (2) can be rewritten as:

$$\varepsilon = \int \left(\sum_{i=1}^N \int K(\mathbf{y} - \mathbf{x}) |I(\mathbf{x}) - b(\mathbf{y})c_i|^2 M_i(\phi(\mathbf{x})) d\mathbf{x} \right) d\mathbf{y} \quad (4)$$

The Heaviside function is defined as follows:

$$H_\epsilon(x) = \frac{1}{2}(1 + \frac{2}{\pi} \arctan(\frac{x}{\epsilon})) \quad (5)$$

The above defined energy ε in Eq. (4) is used as the data term in the energy of the following variational level set formulation:

$$E^{BC}(\phi, \mathbf{c}, b) = \varepsilon(\phi, \mathbf{c}, b) + \nu L(\phi) + \mu R(\phi) \quad (6)$$

ε in Eq. (6) represents the energy term, L represents the length term and R represents the distance regularization term. Minimizing the energy functional E^{BC} with respect to ϕ by using the standard gradient descent method, we obtain the variational level set formulation as follows:

$$\frac{\partial \phi}{\partial t} = -\delta_\phi(\phi)(e_1 - e_2) + \nu \delta(\phi) \operatorname{div}(\frac{\nabla \phi}{|\nabla \phi|}) + \mu \operatorname{div}(d_p |\nabla \phi|) \nabla \phi \quad (7)$$

In Eq. (7), ν and μ are constants. $d_p |\nabla \phi|$ is the diffusion rate of the double well potential function.

In the energy minimization computing process, the optimal c_i and b that minimize the energy ε are expressed as:

$$c_i = \frac{\int (b * K) I M_i(\phi(\mathbf{y})) d\mathbf{y}}{\int (b^2 * K) M_i(\phi(\mathbf{y})) d\mathbf{y}}, i = 1, 2 \quad (8)$$

$$b = \frac{I \sum_{i=1}^N c_i M_i(\phi(\mathbf{y})) * K}{\sum_{i=1}^N c_i^2 M_i(\phi(\mathbf{y})) * K} \quad (9)$$

The above BC model is an effective and excellent algorithm, which provides an idea for the later research of bias field estimation models. However, the BC model has the following problems: 1. The computation of bias field estimation b and c_i has four Gaussian convolution operations in the time iterative process, resulting in too long running time. 2. The BC model is sensitive to uneven illumination images. 3. This model cannot reflect some false targets in the image and has a bad effect on images with intensity inhomogeneity.

The basic idea of the LSACM model is to model the inhomogeneous objects as Gaussian distributions with different means and variances. The computing function of bias field in this model is:

$$b(x) = \frac{\sum_{i=1}^N K_\rho * (I M_i(\phi(x))) \frac{c_i}{\sigma_i^2}}{\sum_{i=1}^N K_\rho * M_i(\phi(x)) \frac{c_i^2}{\sigma_i^2}} \quad (10)$$

The same problem as the BC model is that the convolution in Eq. (10) causes the slow running speed.

Considering these shortcomings, this paper proposes a new bias field estimation function and improves the level set function as well as the energy function. At the same time, we have optimized the algorithm and make some other innovations. Our model is presented in the next section.

3. Proposed model

3.1. Pre-fitting bias field estimation function with K-means++ clustering algorithm

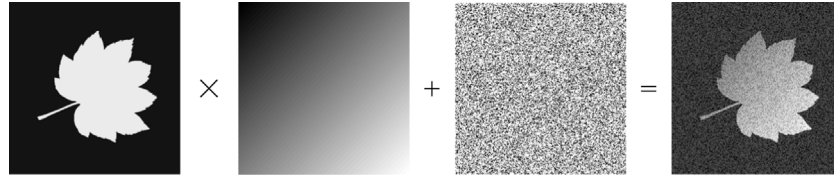
In this paper we propose an active contour model based on K-means++ clustering algorithm (KPBFE). The basic principle of K-means++ clustering algorithm is the initial cluster centers should be as far as possible. The specific steps are as follows:

1. Choose a point x as the first center point c_1 randomly from all input dataset X . Calculate the Euclidean distance $D_i(x)$ between each sample x and the current existing clustering center.

Table 1

Comparative table of prior bias field model works.

Model name	Core idea	Advantages	Imperfection
BC	Local intensity clustering property and local clustering function	Strong robustness to the initial contour	Sensitive to uneven illumination and overmuch convolution
LSACM	Model inhomogeneous objects as Gaussian distributions	High accuracy for intensities inhomogeneous images	Sensitive to initial contour and slow segmentation speed
CLSM	Build a local bias field corrected fitting image energy	Flexible initializations and robustness to noise	Computation of kernel function leads to long segmentation time
EFI	Construct a hybrid region intensity fitting energy functional	Simultaneous segment regions of interest and estimate bias field	Huge convolution results in slow segmentation speed

**Fig. 1.** Illustration of the image model with intensity inhomogeneity. From left to right: the true signal $J(\mathbf{x})$, the bias field function $b(\mathbf{x})$, the noise $n(\mathbf{x})$, and the composite image $I(\mathbf{x})$.

2. Arrange the Euclidean distances of each point randomly and sum up the Euclidean distances squared, which can be written as $\sum_{x \in X} D(x)^2$. Then calculate the probability that each sample is selected as the next clustering center. The probability can be defined by $\frac{D_i(x)^2}{\sum_{x \in X} D(x)^2}$.

3. Repeat process 2 until we get k initial center points $C_i = \{c_1, c_2, \dots, c_k\}$.

4. Recalculate the values $C_i = \frac{1}{|C_i|} \sum_{x \in C_i} x$ for each central object.

5. Finish clustering by using the K-means++ algorithm until the value of C_i no longer changes.

Based on the above K-means++ clustering algorithm, we added a pre-processing process. The input original image I is expanded by the mirror boundary of width w to obtain a new image I' . We set a rectangular frame with size $(2w+1)(2w+1)$ to slide the values on the image I' line by line. Next, compose the data of each line into a new Matrix X with size $m \times (2w+1)(2w+1)$ where m is the number of columns of I . Then n cluster center points B_n are generated for each row of data in the matrix X to obtain a new matrix Y with size $m \times n$. The final value I'' is obtained by repeating the sliding value and the clustering operation j times, where j is the number of lines of the original image I . Due to the pre-processing process, our method takes less time than the original K-means++ clustering algorithm.

With our optimized K-means++ algorithm we define the following bias field estimation model functions:

$$\hat{B}(\mathbf{x}) = Kmeans(I(\mathbf{x})|\mathbf{x} \in \Omega_y) \quad (11)$$

where Ω_y is a small region centered on y in the image domain Ω with size $(2w+1)(2w+1)$. $I(\mathbf{x})$ is the grayscale value of the point \mathbf{x} in the image. $\hat{B}(\mathbf{x})$ reflects the bias field of images with intensity inhomogeneity in the small area Ω_y . $Kmeans$ is the K-means++ clustering algorithm. The bias field b is computed before iteration in the experiment, which saves a lot of time.

3.2. Energy function

For image model in Eq. (1), the purpose of the image segmentation is to divide the image domain Ω into N different regions $\Omega_i, i = 1, \dots, N$. We consider a circular neighborhood with a relatively small radius ρ centered at each point \mathbf{x} in the image domain Ω , which is defined by $O_y \triangleq \{\mathbf{y} : |\mathbf{y} - \mathbf{x}| \leq \rho\}$. $\{\Omega_i\}_{i=1}^N$ induces a partition of the neighborhood O_y according to Assumption (2). For a smooth bias field function, its value $b(\mathbf{x})$ of all \mathbf{x} in O_y can be well approximated by $\hat{B}(\mathbf{x})$. The above reasoning process can be expressed as follows:

On the basis of the image model in Eq. (1), we use the pre-fitting bias field estimation value \hat{B} of Eq. (11) to instead relatively slowly changing bias field b in this paper. Therefore, $b(\mathbf{x})J(\mathbf{x})$ is close to $\hat{B}(\mathbf{x})J(\mathbf{x})$, which can be expressed as:

$$b(\mathbf{x})J(\mathbf{x}) \approx \hat{B}(\mathbf{x})J(\mathbf{x}) \quad (12)$$

With the method about the properties of the real image $J(\mathbf{x})$ piecewise constant, we suppose that there are N disjoint sub-regions in the image domain Ω_i . Then the real image $J(\mathbf{x})$ approximately equals constant c_i in the i sub-region, so $J(\mathbf{x})$ can be approximated by:

$$J(\mathbf{x}) = \sum_{i=1}^N c_i u_i(\mathbf{x}) \quad (13)$$

In Eq. (13), $u_i(\mathbf{x})$ is a membership function. Corresponding to the sub-region Ω_i of the image, $u_i(\mathbf{x})$ is defined as follows:

$$u_i(\mathbf{x}) = \begin{cases} 1, & \mathbf{x} \in \Omega_i \\ 0, & \text{else} \end{cases} \quad (14)$$

Based on the Eq. (1), we propose the following energy function:

$$E(\mathbf{c}) = \sum_{i=1}^N \int_{\Omega} \left| I(\mathbf{x}) - \hat{B}(\mathbf{x})c_i u_i(\mathbf{x}) \right| d\mathbf{x} \quad (15)$$

In Eq. (15) the integral region is over the whole region Ω . By computing region $\Omega_i, i = 1, \dots, N$ and constant $c_i, i = 1, \dots, N$, Eq. (15) can be minimized to complete image segmentation. The level set function of the energy for the cases of $N = 2$ called two-phase formulation. Next we consider the situation of two-phase. The level set function is a function with positive and negative signs in the level set method, which can be used to represent two disjoint regions of region Ω : Ω_1, Ω_2 . Region Ω_1 and Ω_2 can be defined by $M_1(\phi) = H(\phi)$ and $M_2(\phi) = 1 - H(\phi)$ respectively. Where $H(\phi)$ is Heaviside function. Then Eq. (15) can be rewritten as follows:

$$E(\phi, \mathbf{c}) = \int \sum_{i=1}^2 \left| I(\mathbf{x}) - \hat{B}(\mathbf{x})c_i \right| M_i(\phi(\mathbf{x})) d\mathbf{x} \quad (16)$$

For fixed ϕ , the optimal solution c_i that minimizes energy $E(\phi, \mathbf{c})$ can be expressed as:

$$\hat{c}_i = \frac{\int I(\mathbf{x}) M_i(\phi(\mathbf{x})) d\mathbf{x}}{\int \hat{B}(\mathbf{x}) M_i(\phi(\mathbf{x})) d\mathbf{x}}, i = 1, 2 \quad (17)$$

Here \mathbf{c} takes into account the mean values of the outer and inner contour lines in the case of bias field.

3.3. Gradient descent flow function

The above defined Eq. (16) is used as the data term in the energy of the proposed variational level set formulation, which is defined by

$$F^{KPBFE}(\phi, \mathbf{c}) = E(\phi, \mathbf{c}) \quad (18)$$

To minimize the energy functional $F^{KPBFE}(\phi, c)$ according to ϕ with the standard gradient descent method, we transform the energy function into the following variational level set function:

$$\frac{\partial \phi}{\partial t} = -\frac{\partial F^{KPBFE}}{\partial t} = -\delta_\epsilon(\phi) \left(|I(\mathbf{x}) - \hat{B}(\mathbf{x})c_1| - |I(\mathbf{x}) - \hat{B}(\mathbf{x})c_2| \right) \quad (19)$$

where $\delta_\epsilon(\phi)$ is the Dirac function:

$$\delta_\epsilon(\phi) = \frac{\epsilon}{\pi(\epsilon^2 + \phi^2)} \quad (20)$$

The data driven term $|I(\mathbf{x}) - \hat{B}(\mathbf{x})c_1| - |I(\mathbf{x}) - \hat{B}(\mathbf{x})c_2|$ in the gradient flow function uses the absolute value of the difference, which is different from the data driven term in the general model. There are variety of images and the contrast of different images is greatly different in the experiment. So the value of the data driven term in Eq. (19) is greatly different to increase the difficulty of segmentation (Dong et al., 2019). To this end, we rewrite Eq. (19) to limit the magnitude of the data driven term. This new function is effective for increasing the sensitivity of the data driven term at the crossing of zero point. The optimized variational level set function is given by:

$$\frac{\partial \phi}{\partial t} = -\alpha \delta_\epsilon(\phi) \arctan((|I(\mathbf{x}) - \hat{B}(\mathbf{x})c_1| - |I(\mathbf{x}) - \hat{B}(\mathbf{x})c_2|)/\tau) \quad (21)$$

where τ is an adaptive function based on image standard deviation:

$$\tau = \frac{1}{2} \sqrt{\frac{1}{(N-1)(M-1)} \sum_{y=1}^N \sum_{x=1}^M (I(x, y) - \bar{I}(x, y))^2} \quad (22)$$

where N and M are the number of rows and columns of the image matrix respectively. α is a constant and arctan function is used to effectively control and smooth the magnitude of data driven term. Compared with the level set function in the BC model, there is only one energy term in Eq. (21). The adaptive function τ can adjust slope and makes the value of the data driven term remained stable adaptively based on the discrete situation of image data. c_1 and c_2 represent the gray mean of the outer and inner regions of the curve in Eq. (17).

In order to effectively perform robust regularization (Jin and Weng, 2019) on the level set function, we use the following regularization function:

$$\phi_R = \frac{2}{\pi} \arctan(\eta \phi^{n+1}) \quad (23)$$

where η is a setting constant. In Eq. (23), we suppress the slope at both ends by increasing the slope at the crossing of zero point. Compared with previous methods, this regularization function is not only effective, but also has no coefficients that need to be adjusted repeatedly.

In the process of minimizing F^{KPBFE} , curve C contains all the dividing lines on the edge of the image. However, there will be some redundant curves at the non-edge. In this paper we adopt the average filter method (Dong et al., 2019; De Araujo et al., 2016). The method is defined as follows:

$$\bar{\phi}_R = A(k) * \phi_R \quad (24)$$

where $A(k)$ is an average filter with size $(2k+1)(2k+1)$. Average filter can act as the traditional length item $L(\phi)$ and filter the noise.

3.4. Relation to other models

In this section, we explain the relationships of our method with three representative active contour models, including the CV model (Chan and Vese, 1977), the BC model and the LIF model (Zhang et al., 2010).

The function of clustering center point c_1 and c_2 are computed respectively with two following functions:

$$c_1 = \frac{\int_{\Omega} I(\mathbf{x}) \cdot H_\epsilon(\phi(\mathbf{x})) d\mathbf{x}}{\int_{\Omega} H_\epsilon(\phi(\mathbf{x})) d\mathbf{x}} \quad (25)$$

$$c_2 = \frac{\int_{\Omega} I(\mathbf{x}) \cdot [1 - H_\epsilon(\phi(\mathbf{x}))] d\mathbf{x}}{\int_{\Omega} [1 - H_\epsilon(\phi(\mathbf{x}))] d\mathbf{x}} \quad (26)$$

c_1 and c_2 are only related to the global gray value of the image in the above two functions. The segmentation result will be wrong when the gray value inside and outside curve C is different. Our Eq. (17) includes the external and internal average values of the contour line in the case of bias field estimation. Therefore, our computing function is a special form of the function in the CV model.

The BC model introduces a kernel function $K(y - x)$ in Eq. (2) to compute the energy function, which leads to more time spent. Our Eq. (16) does not use a kernel function so that our method has a faster speed. In addition, the BC model also uses a convolution operation in Eq. (9), which increases the segmentation time as well. The convolution operation is not adopted in our function. Compared with the BC model, our model has a faster calculation speed.

Zhang et al. proposed a method to regularize the level set function by a Gaussian kernel. The function they used is as following:

$$\phi = G_\zeta * \phi \quad (27)$$

where ζ is the standard deviation. This method effectively smooth the outline while causes the level set function to be too flat. However, it is not conducive to the determination of the boundary. The Eq. (23) in our paper can effectively solve this problem mainly because arctan function can effectively control and smooth the magnitude of data driven term.

4. Experiments

4.1. Implementation

In this section, we will segment several groups of images with the proposed KPBFE model to test its effect. We also compare our model with some classic models to show advantages. The proposed model will be experimented in MATLAB R2015b on a 2.6-GHz Inter Core i5 personal computer. Unless otherwise specified, the parameters are fixed as $w = 11$, $k = 7$, $\alpha = 1$, $\eta = 10$, $\epsilon = 1$, $\Delta t = 1$ and $c_0 = 1$. N means the iterations number. The complete algorithm steps is:

Step1. Initial the level set function ϕ_0 as:

$$\phi_0 = \begin{cases} -c_0, & x \in \Omega_0 - \partial\Omega_0 \\ 0, & x \in \partial\Omega_0 \\ c_0, & x \in \Omega - \Omega_0 \end{cases} \quad (28)$$

where c_0 is a constant which is greater than 0, Ω_0 is a sub-region of image domain Ω and $\partial\Omega_0$ is the boundary of Ω_0 .

Step2. Compute pre-fitting bias field estimation $\hat{B}(\mathbf{x})$ according to Eq. (11).

Step3. Compute \hat{c}_1 and \hat{c}_2 according to Eq. (17).

Step4. Use Eq. (21) to compute gradient descent flow.

Step5. Regularization and average filtering computation are performed on the level set functions according to Eqs. (23) and (24).

Step6. Output final segmentation results.

The images of The Berkeley Segmentation Dataset and Benchmark used (BSDS) used in this section can be downloaded at <https://www2.eecs.berkeley.edu/Research/Projects/CS/vision/bsds/>

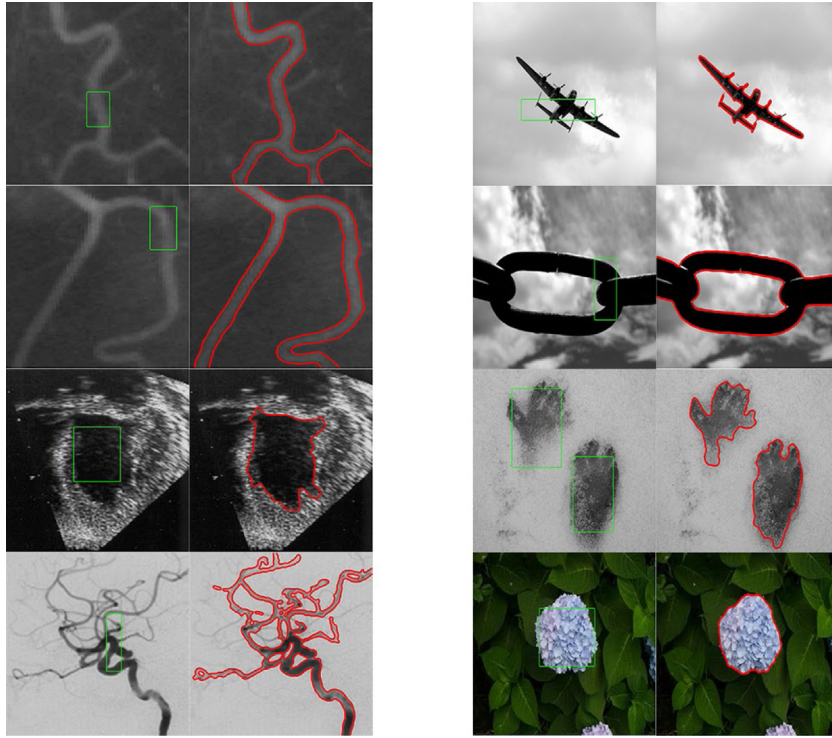


Fig. 2. Segmentation experiments results. The left line is the initial image. The green line is the initial contour. The red line is the segmentation result. (For interpretation of the references to color in this figure legend, the reader is referred to the web version of this article.)

4.2. Segmentation experiments

In this section, eight real and composite images with typical intensity inhomogeneity, low contrast or weak boundary are selected to be segmented by the proposed model. Parameters are set above. As shown in Fig. 2, the left image is the original image with the initial contour. The right image is the segmentation result in each groups of images. It can be seen from the experiment results that the segmentation results of the proposed model are ideal and accurate. That is to say, our model can effectively deal with images with intensity inhomogeneity.

4.3. Contrast experiments

4.3.1. Contrast experiment with classic active contour models

In this section, we compare our model with six classical active contour models, including the RSF model (Li et al., 2008), the LIF model (Zhang et al., 2010), the LGDF model (Wang et al., 2009), the LRCV (Liu and Peng, 2012) model, the LPF (Ding et al., 2018) model and the LoG (Ding et al., 2017) model. The contrast images are six color natural images. Algorithm execution and parameter setting are referred to their respective literature in these traditional models. Parameter setting for each model are as follows: In the RSF model, $c_0 = 2$, $\varepsilon = 1$, $\sigma = 3$, $\lambda_1 = 1$, $\lambda_2 = 1$, $\mu = 1$, $\nu = 0.001 \times 255^2$, $\Delta t = 0.1$. In the LIF model, $c_0 = 1$, $\varepsilon = 0.75$, $\sigma = 3$, $\Delta t = 0.01$, regularized Gauss kernel function with standard deviation 0.75 and size 5×5 . In the LGDF model, $c_0 = 2$, $\varepsilon = 1$, $\sigma = 5$, $\alpha = 30$, $\lambda_1 = 1$, $\lambda_2 = 1$, $\mu = 1$, $\nu = 0.001 \times 255^2$, $\Delta t = 0.1$. In the LRCV model, $c_0 = 1$, $\varepsilon = 1$, $\sigma = 3$, $\lambda_1 = 1$, $\lambda_2 = 1$, $\Delta t = 0.1$. In the LoG model, $c_0 = 2$, $\varepsilon = 1$, $\sigma = 3$, $\delta = 20$, $\lambda_1 = 1$, $\lambda_2 = 1$, $\mu = 2$, $\nu = 0.002 \times 255^2$, $\Delta t = 0.05$. In the LPF model, $c_0 = 1$, $\varepsilon = 1$, $\sigma = 3$, $\lambda_1 = 1$, $\lambda_2 = 1$, $\mu = 1$, $\nu = 0.01 \times 255^2$, $\Delta t = 0.05$.

Experiment results are shown in Fig. 3. The first column of each group represents the original image and initial contour. The second to eighth columns represent the segmentation results of the six images corresponding to each model. Table 2 list running time for each image shown in Fig. 3. The accuracy of experimental results were estimated

Table 2

The time spent for each image shown in Fig. 3. (Time (s)).

Image	RSF	LIF	LGDF	LRCV	LOG	LPF	KPBFE
Img1	6.34	3.07	22.37	2.94	12.40	3.85	0.82
Img2	7.98	4.35	15.61	3.54	23.26	6.87	1.02
Img3	14.23	14.96	13.96	4.89	30.31	13.91	1.37
Img4	33.88	21.35	51.28	4.09	29.05	21.59	3.31
Img5	38.22	5.91	16.34	5.58	34.18	21.84	4.86
Img6	11.97	5.28	10.62	4.49	19.86	6.70	1.54

Table 3

DSC for images shown in Fig. 3.

Image	RSF	LIF	LGDF	LRCV	LOG	LPF	KPBFE
Img1	0.8067	0.3839	0.9391	0.9240	0.6324	0.5878	0.9521
Img2	0.7091	0.9687	0.9182	0.9542	0.9638	0.9672	0.9776
Img3	0.3416	0.9225	0.3904	0.9037	0.9515	0.9184	0.9614
Img4	0.6407	0.8287	0.8162	0.4251	0.8006	0.8634	0.9685
Img5	0.9043	0.7573	0.9497	0.2981	0.8723	0.4473	0.9642
Img6	0.9639	0.9627	0.9579	0.9285	0.9604	0.9754	0.9835

based on the Dice Similarity Coefficient (DSC) (Shattuck et al., 2001). DSC is defined as:

$$DSC = \frac{2(S_a \cap S_b)}{S_a + S_b} \quad (29)$$

where S_a represents the ground truth region obtained manually and S_b represents the object region obtained by experiments. The more the value of DSC close to 1, the higher the accuracy of segmentation. Table 3 and Fig. 4 show the DSC of each images in Fig. 3. It can be seen that the results of other models are mostly inaccurate and even wrong while our model can achieve ideal and accurate results. Therefore, compared with these models, our model has better segmentation results, especially for images with intensity inhomogeneity.

4.3.2. Contrast experiments with two bias field models

We compare our model with two classical bias field estimation models in this section, including the BC model and the LSACM model.

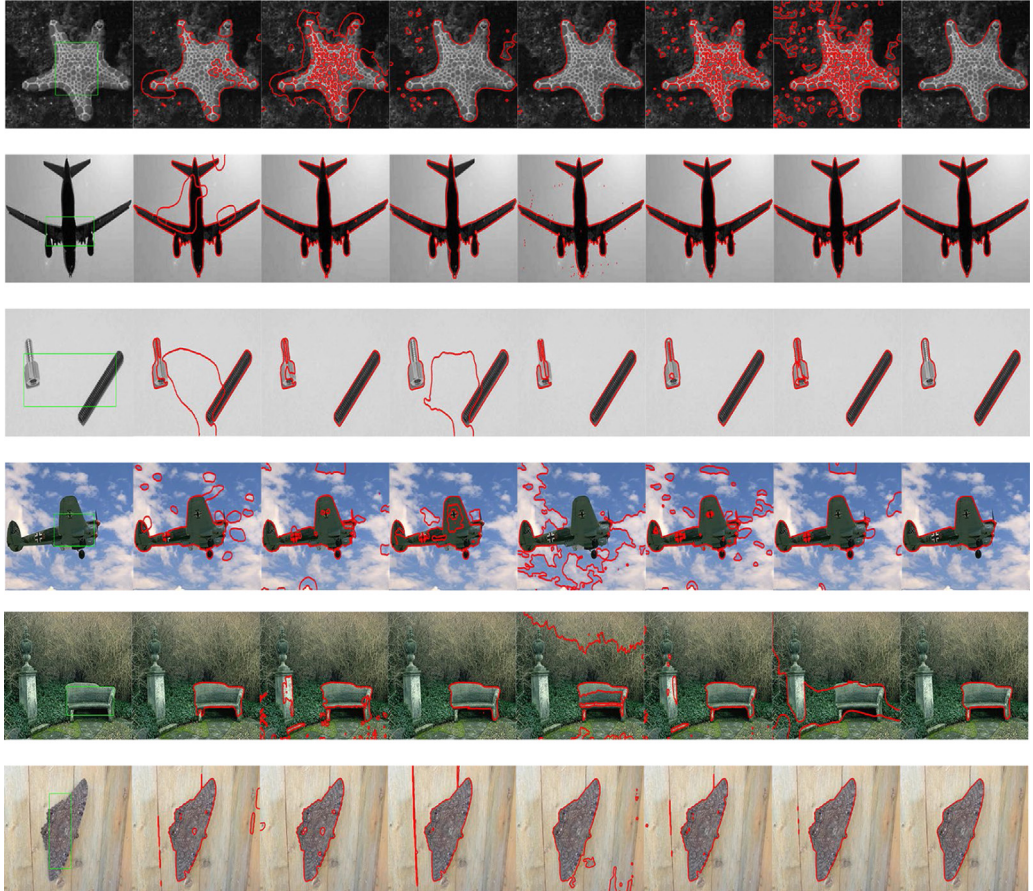


Fig. 3. Contrast experiments results with color natural images. From left to right: original images with corresponding initial contours, results of the RSF model, the LIF model, the LGDF model, the LRCV model, the LoG model, the LPF model and the proposed KPBFE model. The green line is the initial contour. The red line is the segmentation result. (For interpretation of the references to color in this figure legend, the reader is referred to the web version of this article.)

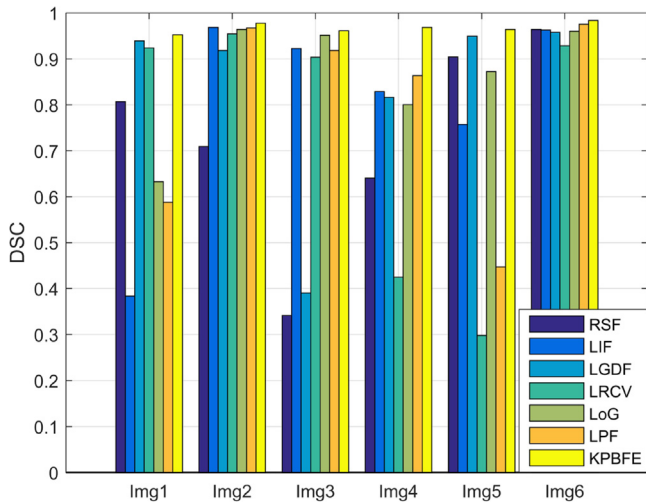


Fig. 4. The DSC of each image shown in Fig. 3.

Fig. 5 shows the segmentation results for each model. **Table 4** shows the time and DSC for each model. **Fig. 6** is the bar chart of DSC. The results in **Fig. 5** and **Table 4** show that the proposed model is more effective than these two bias field models. Pre-fitting bias field computation make our model run faster and variational level set function ensure the accuracy of the segmentation.

Table 4

The time spent and DSC of the **Fig. 5** in the three models. (Time (s)/DCS).

Image	BC	LSACM	KPBFE
Img I (680 × 1020)	13.31/0.5561	70.30/0.8285	6.12/0.8978
Img II (680 × 1020)	8.87/0.6116	105.47/0.6769	4.20/0.9809
Img III (960 × 640)	5.81/0.3763	151.63/0.5932	3.60/0.9244
Img IV (960 × 640)	4.79/0.7792	87.80/0.9821	3.36/0.9851
Img V (960 × 720)	9.39/0.8177	28.04/0.8862	4.76/0.9584
Img VI (960 × 640)	9.21/0.6411	70.94/0.7851	4.71/0.9542

5. Discussion

5.1. About robustness to initialization and noise

We choose two groups of images and set three different initial contours to discuss the robustness of the proposed model to initialization and noise. Meanwhile, Gaussian noise, Salt and pepper noise, Poisson noise and Speckle noise are added to estimate the robustness of our model. Results in **Fig. 7** attest that the position of the initial contour has little influence on the segmentation results. That is to say, the proposed model has strong robustness to initialization. At the same time, each similar image segmentation results under four noise interference show that our model has good robustness to different kinds of noise. This is mainly because the effect of energy limit of the arctan function. Meanwhile, adaptive function τ makes data driven term to remain stable.

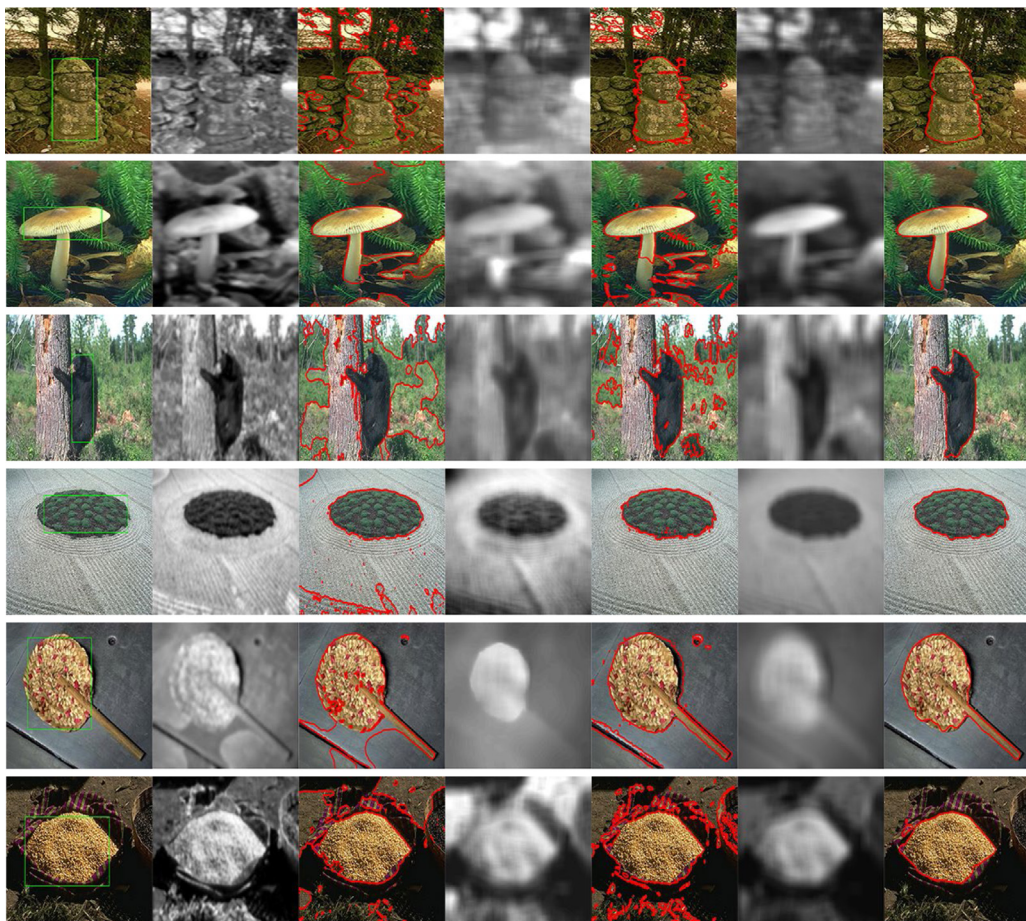


Fig. 5. Contrast experiment results with two bias field models. First column: original images with corresponding initial contours. Second and Third columns: bias fields and segmentation results computed by the BC model. Fourth and Fifth columns: bias fields and segmentation results computed by the LSACM model. Sixth and Seventh columns: bias fields and segmentation results computed by the proposed model.

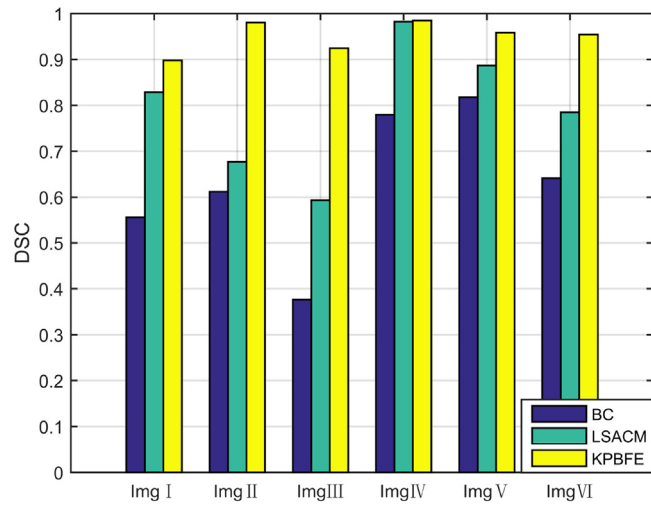


Fig. 6. The bar chart of DSC in Fig. 5.

5.2. About clustering algorithms

The computation time of bias field estimation takes a large proportion in the whole iteration operation. Therefore, we need to choose an appropriate clustering algorithm to improve the computing speed of bias field. K-means clustering algorithm (Dhanachandra et al., 2015) is

Table 5
The time spent and DSC of the Fig. 8 in three clustering algorithms. (Time (s)/DCS).

Image	FCM	K-means	K-means++
a(103 × 97)	0.638/0.9814	1.838/0.9810	0.549/0.9816
b(139 × 130)	1.110/0.9105	1.653/0.9368	0.968/0.9571
c(120 × 97)	0.661/0.9653	1.181/0.9685	0.497/0.9706

relatively dependent on the selection of initial center point. If the initial point is not suitable, it will greatly affect the final clustering result. We choose K-means++ algorithm (Arthur and Vassilvitskii, 2006) and make some optimization in Section 3.1 to reduce the influence of randomness effectively. As a comparison, FCM clustering algorithm (Yang and Nataliani, 2017) is also considered. Fig. 8 shows the segmentation results of three clustering algorithms on a same picture. Table 5 shows the comparison of time spent and accuracy of the three algorithms. Our optimized K-means++ algorithm used in the proposed model is not only faster than the others, but also ensure the accuracy of segmentation.

5.3. About the adjustment of parameters

For normal images, the parameters in the proposed model are set according to the default parameters in Section 4.1. While several parameters need to be adjusted according to the actual image information, such as window size parameter of the bias field estimation w , window size parameter of the average filter k and constant α in variational level set function. In our experiment, we adjust w from 7 to 17, k from 3 to 11 and α from 1 to 2. In the first row of Fig. 9, w and k

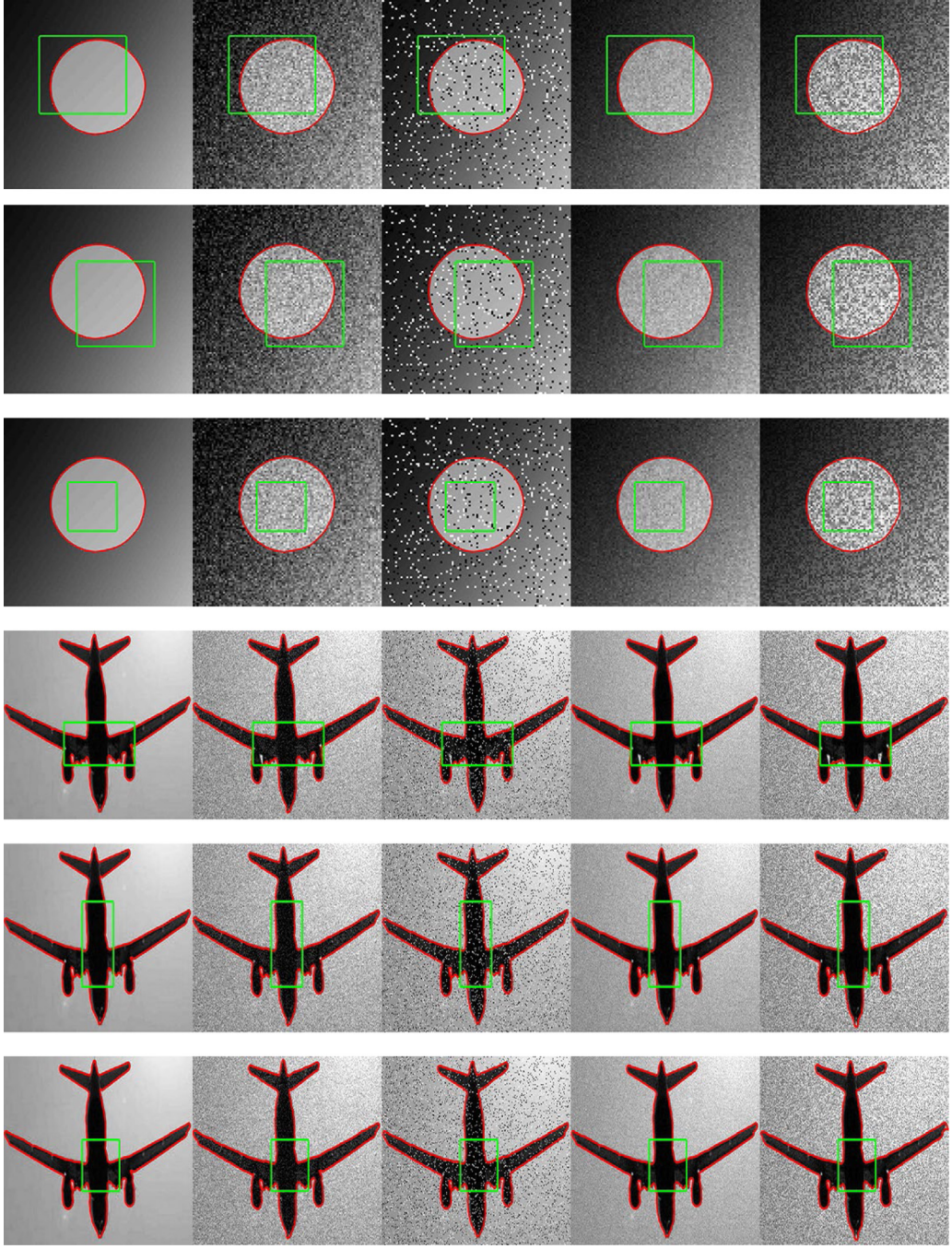


Fig. 7. Robustness experiment results by the proposed model under different initial contours and four kinds of noise. From left to right: final results of initial images, images corrupted by Gaussian noise, Salt and pepper noise, Poisson noise and Speckle noise, respectively.

need to be enlarged appropriately when segment a large target. For small images or small targets, such as the images in the second row, w and k should be reduced. α is used to limit the amplitude and control the convergence rate of segmentation. The results in the third row shows that increasing the value of α can accelerate the convergence of segmentation when the number of iterations remains unchanged.

5.4. About adaptive function τ

The adaptive function τ in Eq. (22) can improve the slope and make the data driven term has better performance. In Eq. (22) the standard deviation of grayscale image is the arithmetic square root of variance and it represents the dispersion degree of image, which means the distance between the value of target and the mean value. The smaller

the standard deviation, the more aggregated the data. Conversely, the more discrete the data. Compared with the fixed τ , adaptive τ can adaptively be adjusted to the discrete situation of image data and make data driven energy remained stable. Fig. 10 shows contrast experiment between fixed τ and adaptive τ . We set two fixed τ ($\tau = 2$ and $\tau = 10$) to compare the effects of fixed τ and adaptive τ on segmentation accuracy. We compute that $\tau = 2.4038$ in Img1 and $\tau = 4.0381$ in Img2 by Eq. (22). The results listed in Table 6 show that the adaptive τ has better segmentation accuracy.

5.5. About the arctan function in energy function

In Eq. (21) the purposes of using arctan function are as follows: (1) Effectively control and smooth the magnitude of data driven term. (2)

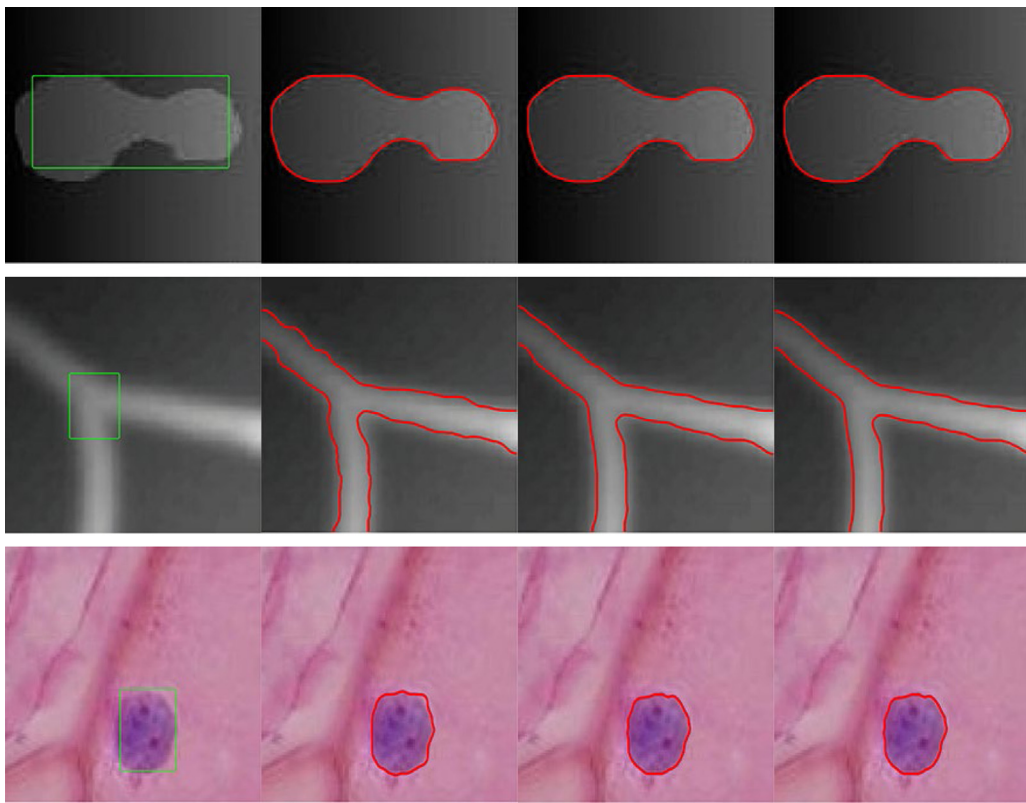


Fig. 8. Clustering algorithms segmentation results under three different clustering algorithms. From left to right: original images with initial contours, segmentation results by the proposed model with the FCM clustering algorithm, standard K-means algorithm and optimized K-means++ algorithm.

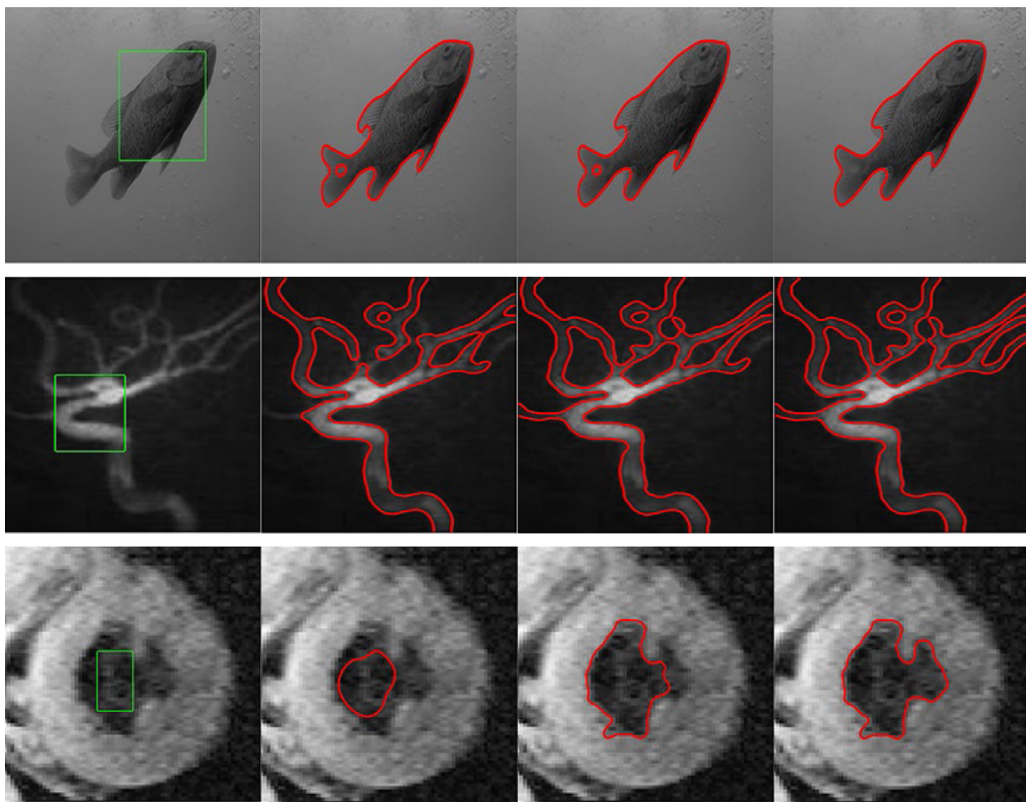


Fig. 9. Experiment results under different parameters. The parameters in the first row are set as: $w = 11, k = 7; w = 13, k = 9; w = 13, k = 11$. The parameters in the second row are set as: $w = 11, k = 7; w = 11, k = 5; w = 9, k = 5$. The parameters in the second row are set as: $\alpha = 1.5; \alpha = 1.75; \alpha = 2$ while retains $N = 55$.

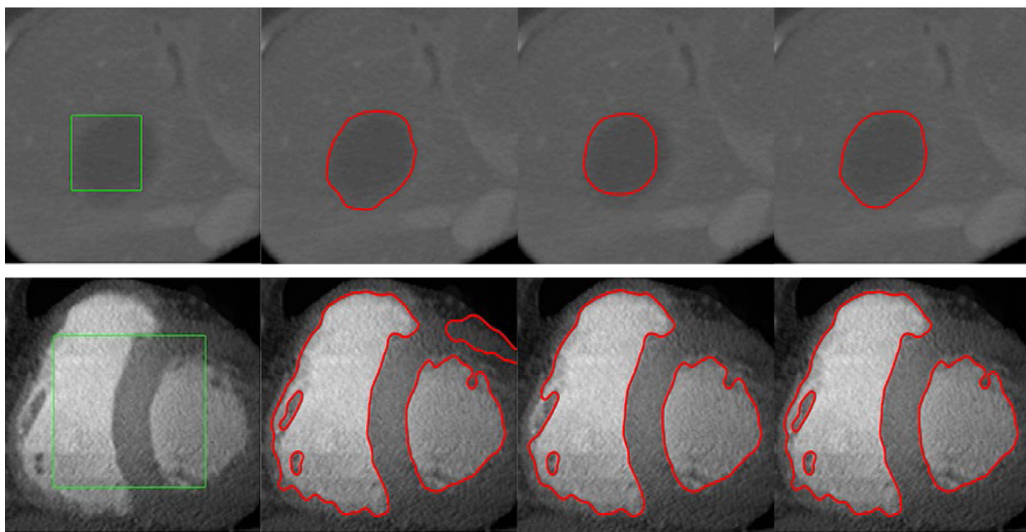


Fig. 10. Contrast experiment between fixed τ and adaptive τ . From left to right: original images with initial contours, segmentation results by $\tau = 2$, $\tau = 10$ and adaptive τ ($\tau = 2.4038$ in Img1 and $\tau = 4.0381$ in Img2).

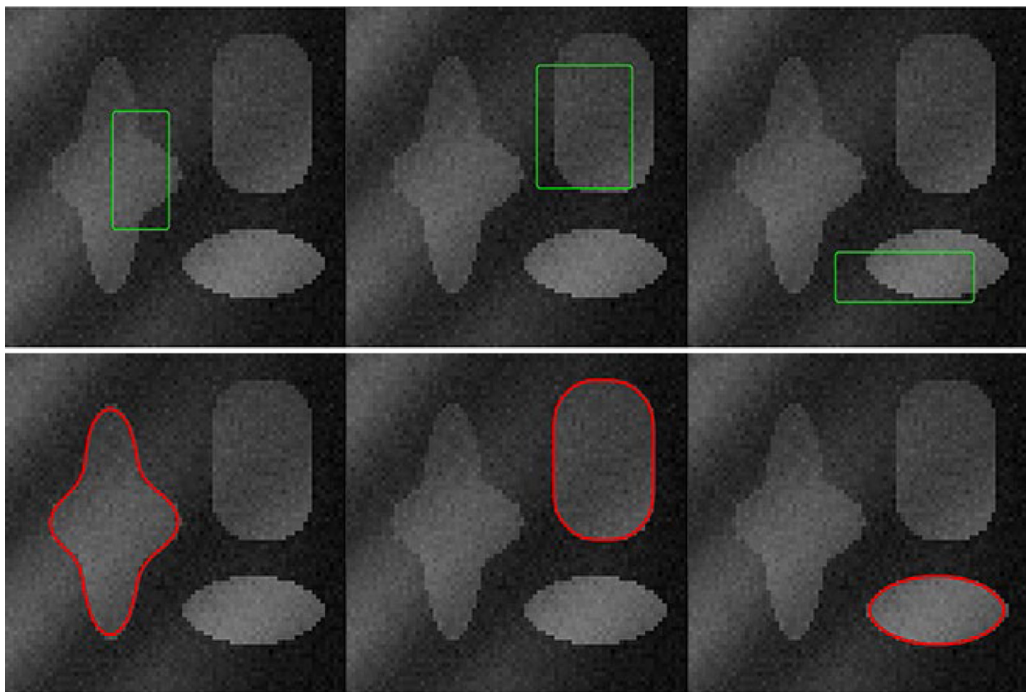


Fig. 11. Segmentation results by the proposed model under different initial contours. First row: three different initial contours. Second row: segmentation results.

Table 6

The DSC of the Fig. 10 with different τ . (DCS).

Image	$\tau = 2$	$\tau = 10$	Adaptive τ
ImgA(103 × 97)	0.9496	0.8098	0.9565
ImgB(139 × 130)	0.9459	0.9671	0.9743

Limit the range of data driven term. (3) Improve the sensitivity of data driven term at crossing point of zero. Since arctan function is used to limit the segmentation range, the segmentation target can be arbitrarily selected by the proposed model. The specified segmentation results can be obtained by setting different initial contours in Fig. 11.

Meanwhile, we compare the segmentation results of the gradient descent flow function with arctan function and without arctan function in this section. We define the following function without arctan function:

$$\frac{\partial \phi'}{\partial t} = -\alpha \delta_\epsilon(\phi)(|I(x) - \hat{B}(x)c_1| - |I(x) - \hat{B}(x)c_2|)/\tau \quad (30)$$

Fig. 10 shows the segmentation results of two gradient descent function. It can be concluded that the proposed model is easy to fall into the false targets when there is no arctan function to limit the data driven term. Therefore the arctan function obtains a better segmentation effect (see Fig. 12).

6. Conclusions

In this paper, we propose a new active contour model (KPBFE) to overcome the shortcomings of classical bias field estimation model. We cluster multivariable data and take the clustering center point

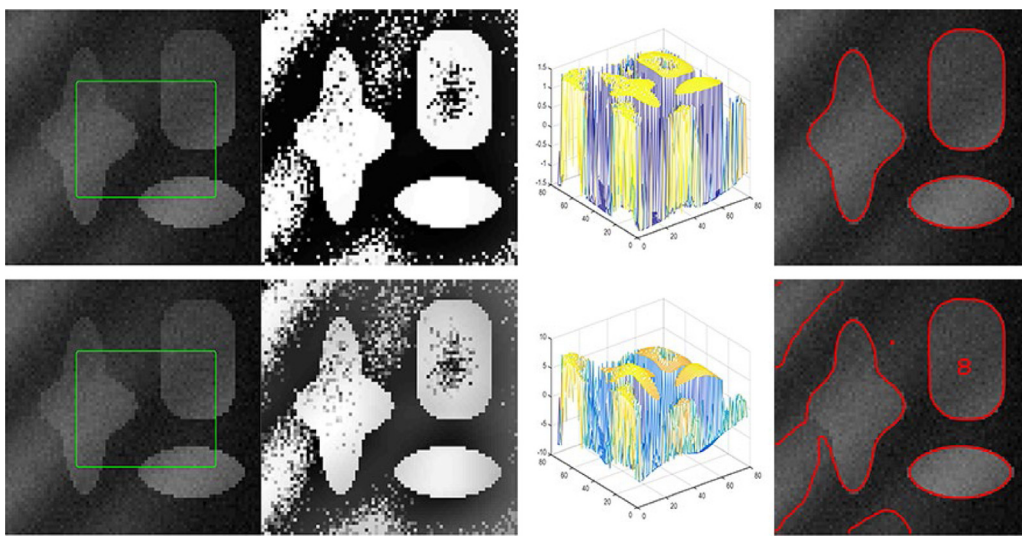


Fig. 12. The segmentation results by two different gradient descent flow functions. The first row is the results with arctan function and the second row is the results without arctan function. From left to right: original images with initial contours, data driven term, three-dimensional mesh maps of the data driven term, final results.

as bias field b with our optimized K-means++ clustering algorithm. The computation method of clustering center points takes the average value of the grayscale inside and outside the contour of the bias field estimation into account. Due to an adaptive function τ , we optimize the variational level set function and limit the magnitude of the data driven term effectively. There is a pre-processing that we complete computing bias field b before the iteration and there is no more time-consuming convolutions operation in the whole computing process. Therefore the computing speed is greatly increased. Experiments results show that our model has faster segmentation speed and better robustness on the images with intensity inhomogeneity. But it should be noted that we only apply the proposed model for segmentation of two-phase images. In the future work, we will consider using multiple level set functions and deep-learning based method to further improve our model. For objects with obvious multiple colors, the core problem is how to construct the characteristic functions of different regions. We will work on using multiple level set functions on the basis of the proposed model and attaching corresponding constraints. Self Organizing Maps (SOM) is an effective clustering algorithm based on neural network (Abdelsamea et al., 2015). We will study the feasibility of using SOM clustering algorithm to compute local clustering center in the future.

CRediT authorship contribution statement

Guirong Weng: Conceptualization, Methodology, Software, Resources, Writing - review & editing, Supervision, Project administration, Funding acquisition. **Bin Dong:** Validation, Formal analysis, Investigation, Data curation, Writing - original draft, Visualization.

Declaration of competing interest

The authors declare that they have no known competing financial interests or personal relationships that could have appeared to influence the work reported in this paper.

Acknowledgments

This work is supported by the National Nature Science Foundation of China [grant No. 61873176, No. 61473201] and Postgraduate Research & Practice Innovation Program of Jiangsu Province, China [grant No. KYCX19_1928].

References

- Abdelsamea, M.M., Gnecco, G., Gaber, M.M., 2015. An efficient self-organizing active contour model for image segmentation. Neurocomputing 149, 820–835. <http://dx.doi.org/10.1016/j.neucom.2014.07.052>.
- Arthur, D., Vassilvitskii, S., 2006. K-means++: The advantages of careful seeding. Chem. Eng. 8, 26–28. <http://dx.doi.org/10.1145/1283383.1283494>.
- Banerjee, A., Maji, P., 2019. Segmentation of bias field induced brain MR images using rough sets and stomped-t distribution. Inf. Sci. (Ny) 504, 520–545. <http://dx.doi.org/10.1016/j.ins.2019.07.027>.
- Cai, Q., Liu, H., Zhou, S., Sun, J., Li, J., 2018. An adaptive-scale active contour model for inhomogeneous image segmentation and bias field estimation. Pattern Recognit. 82, 79–93. <http://dx.doi.org/10.1016/j.patcog.2018.05.008>.
- Çataloluk, H., Çelebi, F.V., 2018. A novel hybrid model for two-phase image segmentation: GSA based Chan-Vese algorithm. Eng. Appl. Artif. Intell. 73, 22–30. <http://dx.doi.org/10.1016/j.engappai.2018.04.027>.
- Chan, T.F., Vese, L.A., 1977. Active contours without edges. Br. Dent. J. 10, 266–277. <http://dx.doi.org/10.1109/83.902291>.
- Chan, S., Yang, X., Chen, G., Pu, J., Shi, D., Wang, L., Chang, Y., 2018. Active contours driven by edge entropy fitting energy for image segmentation. Signal Process. 149, 27–35. <http://dx.doi.org/10.1016/j.sigpro.2018.02.025>.
- Comelli, A., Stefano, A., Russo, G., Bignardi, S., Sabini, M.G., Petrucci, G., Ippolito, M., Yezzi, A., 2019. K-nearest neighbor driving active contours to delineate biological tumor volumes. Eng. Appl. Artif. Intell. 81, 133–144. <http://dx.doi.org/10.1016/j.engappai.2019.02.005>.
- De Araujo, A.F., Constantino, C.E., Tavares, J.M.R.S., 2016. Smoothing of ultrasound images using new selective average filter. Expert Syst. Appl. 60, 96–106. <http://dx.doi.org/10.1016/j.eswa.2016.04.034>.
- Demirhan, A., Güler, I., 2011. Combining stationary wavelet transform and self-organizing maps for brain MR image segmentation. Eng. Appl. Artif. Intell. 24, 358–367. <http://dx.doi.org/10.1016/j.engappai.2010.09.008>.
- Dhanachandra, N., Manglem, K., Chanu, Y.J., 2015. Image segmentation using K-means clustering algorithm and subtractive clustering algorithm. Procedia Comput. Sci. 54, 764–771. <http://dx.doi.org/10.1016/j.procs.2015.06.090>.
- Ding, K., Xiao, L., Weng, G., 2017. Active contours driven by region-scalable fitting and optimized Laplacian of Gaussian energy for image segmentation. Signal Process. 134, 224–233. <http://dx.doi.org/10.1016/j.sigpro.2016.12.021>.
- Ding, K., Xiao, L., Weng, G., 2018. Active contours driven by local pre-fitting energy for fast image segmentation. Pattern Recognit. Lett. 104, 29–36. <http://dx.doi.org/10.1016/j.patrec.2018.01.019>.
- Dong, B., Jin, R., Weng, G., 2019. Active contour model based on local bias field estimation for image segmentation. Signal Process., Image Commun. 78, 187–199. <http://dx.doi.org/10.1016/j.image.2019.07.001>.
- Gamino-Sánchez, F., Hernández-Gutiérrez, I.V., Rosales-Silva, A.J., Gallegos-Funes, F.J., Mújica-Vargas, D., Ramos-Díaz, E., Carvajal-Gámez, B.E., Kinani, J.M.V., 2018. Block-matching fuzzy C-means clustering algorithm for segmentation of color images degraded with Gaussian noise. Eng. Appl. Artif. Intell. 73, 31–49. <http://dx.doi.org/10.1016/j.engappai.2018.04.026>.
- Jin, R., Weng, G., 2019. A robust active contour model driven by pre-fitting bias correction and optimized fuzzy c-means algorithm for fast image segmentation. Neurocomputing 359, 408–419. <http://dx.doi.org/10.1016/j.neucom.2019.06.019>.

- Kass, M., Witkin, A., Terzopoulos, D., et al., 2011. Snakes: Active contour models. *Act. Percept. Robot Vis.* 331, 599–613. http://dx.doi.org/10.1007/978-3-642-77225-2_31.
- Li, Q., Deng, T., Xie, W., 2016. Active contours driven by divergence of gradient vector flow. *Signal Process.* 120, 185–199. <http://dx.doi.org/10.1016/j.sigpro.2015.08.020>.
- Li, Shuo, Fevens, T., Krzyzak, A., Li, Song, 2006. Automatic clinical image segmentation using pathological modeling, PCA and SVM. *Eng. Appl. Artif. Intell.* 19, 403–410. <http://dx.doi.org/10.1016/j.engappai.2006.01.011>.
- Li, C., Gore, J.C., Davatzikos, C., 2014. Multiplicative intrinsic component optimization (MICO) for MRI bias field estimation and tissue segmentation. *Magn. Reson. Imaging* 32, 913–923. <http://dx.doi.org/10.1016/j.mri.2014.03.010>.
- Li, C., Huang, R., Ding, Z., Gatenby, J.C., Metaxas, D.N., Gore, J.C., 2011. A level set method for image segmentation in the presence of intensity inhomogeneities with application to MRI. *IEEE Trans. Image Process.* 20, 2007–2016. <http://dx.doi.org/10.1109/TIP.2011.2146190>.
- Li, C., Kao, C.Y., Gore, J.C., Ding, Z., 2008. Minimization of region-scalable fitting energy for image segmentation. *IEEE Trans. Image Process.* 17, 1940–1949. <http://dx.doi.org/10.1109/TIP.2008.2002304>.
- Li, C., Xu, C., Gui, C., Fox, M.D., 2010. Distance regularized level set evolution and its application to image segmentation. *IEEE Trans. Image Process.* 19, 3243–3254. <http://dx.doi.org/10.1109/TIP.2010.2069690>.
- Liu, C., Liu, W., Xing, W., 2017. An improved edge-based level set method combining local regional fitting information for noisy image segmentation. *Signal Process.* 130, 12–21. <http://dx.doi.org/10.1016/j.sigpro.2016.06.013>.
- Liu, S., Peng, Y., 2012. A local region-based Chan–Vese model for image segmentation. *Pattern Recognit.* 45, 2769–2779. <http://dx.doi.org/10.1016/j.patcog.2011.11.019>.
- Miao, J., Huang, T.Z., Zhou, X., Wang, Y., Liu, J., 2018. Image segmentation based on an active contour model of partial image restoration with local cosine fitting energy. *Inf. Sci. (Ny)* 447, 52–71. <http://dx.doi.org/10.1016/j.ins.2018.02.007>.
- Mousavirad, S.J., Ebrahimpour-Komleh, H., Schaefer, G., 2020. Automatic clustering using a local search-based human mental search algorithm for image segmentation. *Appl. Soft Comput. J.* 96, 106604. <http://dx.doi.org/10.1016/j.asoc.2020.106604>.
- Pham, V.T., Tran, T.T., Shyu, K.K., Lin, C., Wang, P.C., Lo, M.T., 2016. Shape collaborative representation with fuzzy energy based active contour model. *Eng. Appl. Artif. Intell.* 56, 60–74. <http://dx.doi.org/10.1016/j.engappai.2016.08.015>.
- Sarkar, S., Das, S., Chaudhuri, S.S., 2016. Hyper-spectral image segmentation using Rényi entropy based multi-level thresholding aided with differential evolution. *Expert Syst. Appl.* 50, 120–129. <http://dx.doi.org/10.1016/j.eswa.2015.11.016>.
- Shattuck, D.W., Sandor-Leahy, S.R., Schaper, K.A., Rottenberg, D.A., Leahy, R.M., 2001. Magnetic resonance image tissue classification using a partial volume model. *Neuroimage* 13, 856–876. <http://dx.doi.org/10.1006/nimg.2000.0730>.
- Wang, L., He, L., Mishra, A., Li, C., 2009. Active contours driven by local Gaussian distribution fitting energy. *Signal Process.* 89, 2435–2447. <http://dx.doi.org/10.1016/j.sigpro.2009.03.014>.
- Wang, L., Zhu, J., Sheng, M., Cribb, A., Zhu, S., Pu, J., 2018. Simultaneous segmentation and bias field estimation using local fitted images. *Pattern Recognit.* 74, 145–155. <http://dx.doi.org/10.1016/j.patcog.2017.08.031>.
- Wells, W.M., Grimson, W., Kikinis, R., Jolesz, F.A., 1995. Adaptive segmentation of MRI data. In: Lect. Notes Comput. Sci. (Including Subser. Lect. Notes Artif. Intell. Lect. Notes Bioinformatics), Vol. 905. pp. 59–69. <http://dx.doi.org/10.1109/42.511747>.
- Wu, C., Kang, Z., 2021. Robust entropy-based symmetric regularized picture fuzzy clustering for image segmentation. *Digit. Signal Process. Rev. J.* 110, 102905. <http://dx.doi.org/10.1016/j.dsp.2020.102905>.
- Yang, M., Nataliani, Y., 2017. Robust-learning fuzzy c-means clustering algorithm with unknown number of clusters. *Pattern Recognit.* 71, 45–59. <http://dx.doi.org/10.1016/j.patcog.2017.05.017>.
- Zhang, K., Song, H., Zhang, L., 2010. Active contours driven by local image fitting energy. *Pattern Recognit.* 43, 1199–1206. <http://dx.doi.org/10.1016/j.patcog.2009.10.010>.
- Zhang, K., Zhang, L., Lam, K.M., Zhang, D., 2016. A level set approach to image segmentation with intensity inhomogeneity. *IEEE Trans. Cybern.* 46, 546–557. <http://dx.doi.org/10.1109/TCYB.2015.2409119>.
- Zhou, Y., Shi, W., Chen, W., Chen, Y., Li, Y., Tan, L., Chen, D., 2015. Active contours driven by localizing region and edge-based intensity fitting energy with application to segmentation of the left ventricle in cardiac CT images. *Neurocomputing* 156, 199–210. <http://dx.doi.org/10.1016/j.neucom.2014.12.061>.
- Zhou, S., Wang, J., Zhang, M., Cai, Q., Gong, Y., 2017. Correntropy-based level set method for medical image segmentation and bias correction. *Neurocomputing* 234, 216–229. <http://dx.doi.org/10.1016/j.neucom.2017.01.013>.